Chapter 6

Incorporating recent theoretical advances on transport coefficients in a time-dependent modulation model

6.1 Introduction

As discussed in the previous chapter, the compound model of *Ferreira and Potgieter* (2004) is based on an empirical approach where model results are compared to observations in order to construct a realistic time-dependence in the transport coefficients. This was done because of a lack of a clear theory on how the diffusion and drift coefficients should change over a solar cycle. However, recent progress by *Teufel and Schlickeiser* (2002, 2003), *Shalchi et al.* (2004), *Minnie et al.* (2007) and *Engelbrecht* (2008) gives a much clearer picture of how the diffusion coefficients depend on basic turbulence quantities, such as the magnetic field magnitude and variance, which change over a solar cycle.

In this chapter these new theories, which have never been tested time-dependently, is introduced in a numerical model to calculate long-term time-dependent cosmic ray modulation. The well established 2D time-dependent modulation model (e.g. *Le Roux and Potgieter*, 1995; *Ferreira and Potgieter*, 2004; *Ndiitwani et al.*, 2005) as discussed in Chapter 4, is used and model results are compared to Voyager 1, Ulysses and IMP 8 observations.

In order to test these recent theories, a detailed study of various parameters which may effect cosmic ray modulation over different solar cycles is done. To construct a time-dependence in the transport coefficients, time-dependent changes in basic turbulence quantities such as the magnetic field magnitude and magnetic field variance as well as the tilt angle at Earth are transported out into the heliosphere in the model. It will be shown that this results in realistic modulation on a global scale when compared to observations depending of course on what set of parameters is assumed. In this chapter various parameters like the cosmic ray modulation boundary (heliopause) position, TS position, HPS, diffusion and drift coefficients are varied and their effects on computed cosmic ray intensities along the Voyager 1 spacecraft trajectory and at Earth are illustrated.

It is shown that after incorporating the recent theoretical advances mentioned above, the model produces results which are compatible to observations along the Voyager 1 trajectory and at Earth. However, the model fails to reproduce observations at Earth for some periods, especially from ∼2004 onwards, although the results are largely compatible with observations at Earth from ∼1985 to ∼2004. It will be shown in detail that even after varying most of the important model parameters, the model cannot reproduce the observations at Earth for the period ∼2004 onwards. As will be argued in the next chapter that in order to fit the data at Earth from ∼2004 onwards, a different time-dependence in the diffusion coefficients (not drifts) are needed.

6.2 New theoretical advances in the transport coefficients

Of primary importance to cosmic ray modulation is the coupling of the transport parameters, mentioned in Chapter 3, to the background field and magnetic turbulence (see e.g. *Bieber et al.*, 1994; *Matthaeus et al.*, 2003; *Bieber et al.*, 2004; *Shalchi et al.*, 2008). From these theoretical studies of turbulence in the solar wind and cosmic ray diffusion, expressions for the spatial and rigidity dependence can be obtained for the different mean free paths for implementation in the numerical model.

6.2.1 The parallel diffusion coefficient

For the parallel mean free path *Teufel and Schlickeiser* (2002) give an applicable expression for protons (damping model) in the inner heliosphere with rigidity, P, in the range 10^{-1} MV $< P < 10^4$ MV as $\lambda_{||} \propto P^{1/3}$ at Earth (see Chapter 3, Section 3.5). However, in the numerical model which calculates cosmic ray intensities throughout the whole heliosphere, it is assumed that,

$$\lambda_{||} = C_1 \left(\frac{P}{P_0}\right)^{\frac{1}{3}} \left(\frac{r}{r_0}\right)^{C_2} f_2(t) \quad \text{for } r < r_{ts} \tag{6.1}$$

and

$$\lambda_{||} = \frac{C_1}{s_k} \left(\frac{P}{P_0}\right)^{\frac{1}{3}} \left(\frac{r}{r_0}\right)^{C_2} \left(\frac{r_{ts}}{r}\right) f_2(t) \quad \text{for } r \geq r_{ts} \tag{6.2}$$

where $P_0 = 1$ MV, $r_0 = 1$ AU, C_1 (in units of AU) a constant determining the absolute value of the mean free path, C_2 a constant determining the radial dependence, r_{ts} the TS position, s_k the compression ratio and $f_2(t)$ (as given below in Equation 6.5) a dimensionless time-varying function which gives the time-dependence in $\lambda_{||}$ and which is transported from the Earth into the heliosphere and out into the heliosheath with the solar wind speed.

According to *Burlaga et al.* (2007) the Voyager observations of B indicate that $B \propto r$ for $r > r_{ts}$ with r_{ts} the position of the TS in AU. If the diffusion coefficients have some dependence on B, changes over the shock is expected. In this work, Equation 6.1 is valid for $r < r_{ts}$, and

it is assumed that the diffusion (mean free path) decreases as the compression ratio s_k at the shock and then scales as $\propto 1/r$ up to the heliopause, as given by Equation 6.2. To calculate the cosmic ray intensities *Florinski et al.* (2003); *Ferreira and Scherer* (2006); *Ferreira et al.* (2007a,b) made similar assumptions about the diffusion coefficients, assuming that they are inversely proportional to B. Due to flow deceleration of the solar wind, B increases further towards the heliopause after a sudden initial increase over the TS. Note that the re-acceleration of galactic cosmic rays at the solar wind TS is not considered in this approach.

The parallel diffusion coefficient for particles with speed v is given by,

$$K_{||} = \lambda_{||}\frac{v}{3}.$$

The time-dependence of $K_{||}$ ($f_2(t)$ in Equation 6.1) is attained using an intricate expression for $\lambda_{||}$ given by *Teufel and Schlickeiser* (2003) as

$$\lambda_{||} = \frac{3s}{\sqrt{\pi}(s-1)}\frac{R^2}{b_k\ k_{min}}\left(\frac{B}{\delta B_{slab,x}}\right)^2\left[\frac{b_k}{4\sqrt{\pi}} + \frac{2}{\sqrt{\pi}(2-s)(4-s)}\frac{b_k}{R^s}\right] \tag{6.3}$$

where $s = 5/3$, the spectral index of the inertial range derived by Kolmogorov, b_k a fraction of particle to Alfven speed assuming maximum dynamical effects, $k_{min} = 10^{-10}$ m^{-1} the spectral break point between the inertial and energy range on the turbulence power spectrum at 1 AU, $R = k_{min}R_L$, with the Larmor radius $R_L = \frac{P}{Bc}$, c the speed of light and $\delta B^2_{slab,x}$ the x component of the slab variance. The slab variance $\delta B^2_{slab} = 2\delta B^2_{slab,x}$ and when e.g. a 20/80 ratio of slab to 2D variance is assumed (*Bieber et al.*, 1994) $\delta B^2_{slab} = 0.2\delta B^2$ and $\delta B^2_{2D} = 0.8\delta B^2$ where δB^2 is the total variance and δB^2_{2D} the two-dimensional variance.

Only the influence of time varying quantities B and δB^2 on $\lambda_{||}$ is considered and Equation 6.3 can be approximated as

$$\lambda_{||} \propto \left(\frac{1}{\delta B_{slab,x}}\right)^2\left[\frac{1}{4} + \frac{18}{7}\left(\frac{B\ c}{P\ k_{min}}\right)^{5/3}\right]. \tag{6.4}$$

From Equation 6.4 the function $f_2(t)$ (in Equation 6.1) can be deduced as

$$f_2(t) = C_4\left(\frac{1}{\delta B(t)}\right)^2\left[\frac{1}{4} + \frac{18}{7}\left(\frac{B(t)\ c}{P\ k_{min}}\right)^{5/3}\right], \tag{6.5}$$

with C_4 a constant in units of (nT)^2.

6.2.2 The perpendicular diffusion coefficient

For perpendicular diffusion, it was shown using simulations that both can scale as the parallel coefficient (*Le Roux et al.*, 1999; *Giacalone and Jokipii*, 1999; *Qin et al.*, 2002a) so it is assumed that:

$$K_{\perp r} = aK_{||}\frac{f_3(t)}{f_2(t)}, \tag{6.6}$$

and

$$K_{\perp\theta} = bK_{||}F(\theta)\frac{f_3(t)}{f_2(t)}, \tag{6.7}$$

where a is the ratio of perpendicular diffusion coefficient in radial direction to parallel diffusion coefficient, b is the ratio of the perpendicular diffusion coefficient in the polar direction to parallel diffusion coefficient, $F(\theta)$ a function enhancing $K_{\perp\theta}$ towards the poles by a factor of 6 (*Potgieter*, 2000; *Ferreira and Potgieter*, 2004) and $f_3(t)$ (as given below in Equation 6.10) a different time-varying function when compared to $f_2(t)$ and which incorporate solar cycle related changes in these coefficients. Note that, as will be discussed below, $K_{||}$ and $K_{\perp}$ (i.e. $K_{\perp r}$ and $K_{\perp\theta}$) depend differently on magnetic field magnitude and variance and have different functions simulating the time-dependence. Therefore, when $K_{\perp}$ is expressed in terms of $K_{||}$ as above, the expression is divided by $f_2(t)$ to remove the time-dependence of $K_{||}$ and multiplied by $f_3(t)$ to describe the time-dependence of $K_{\perp}$.

For time-dependence in the perpendicular diffusion coefficients, the expression for the perpendicular mean free path $\lambda_{\perp}$ as given by *Shalchi et al.* (2004) is utilised,

$$\lambda_{\perp} \approx \left[\frac{2\nu-1}{4\nu}\, F_2(\nu)\, a_k^2\, \frac{\delta B_{2D}^2}{B^2}\sqrt{3}\, l_{2D}\right]^{\frac{2}{3}} \lambda_{||}^{\frac{1}{3}}. \tag{6.8}$$

Where $\nu = 5/6$ the spectral index of slab/2D model magnetic field, $a_k = \frac{1}{\sqrt{3}}$ a numerical factor, l_{2D} the 2D correlation length, where $l_{2D} = \frac{l_{slab}}{10} = 4.55 \times 10^9$m (here l_{slab} is the slab correlation length) and

$$F_2(\nu) = \sqrt{\pi}\,\frac{\Gamma(\nu)}{\Gamma(\nu-\frac{1}{2})}\frac{2\nu}{2\nu-1}$$

where $\Gamma(\nu) = \int_0^{\infty} x^{\nu-1}e^{-x}dx$ for $\nu > 0$.

Since only the influence of time varying quantities B and δB^2 on $\lambda_{\perp}$ is considered, the expression for $\lambda_{\perp}$ in Equation 6.8 can be approximated as

$$\lambda_{\perp} \propto \left(\frac{\delta B_{2D}}{B}\right)^{\frac{4}{3}} \left(\left(\frac{1}{\delta B_{slab,x}}\right)^2 \left[\frac{1}{4} + \frac{18}{7}\left(\frac{B\,c}{P\,k_{min}}\right)^{5/3}\right]\right)^{\frac{1}{3}}. \tag{6.9}$$

From Equation 6.9 the time-dependence for the perpendicular diffusion coefficients, which is described by the function $f_3(t)$ in Equations 6.6 and 6.7, can be deduced as

$$f_3(t) = C_5\left(\frac{\delta B(t)}{B(t)}\right)^{\frac{4}{3}} \left(\left(\frac{1}{\delta B(t)}\right)^2 \left[\frac{1}{4} + \frac{18}{7}\left(\frac{B(t)\,c}{P\,k_{min}}\right)^{5/3}\right]\right)^{\frac{1}{3}} \tag{6.10}$$

with C_5 a constant in units of $(\text{nT})^{2/3}$.

6.2.3 The drift coefficient

Concerning drifts, recent theoretical work done by *Minnie et al.* (2007) showed that changes in δB over a solar cycle can affect the drift coefficient K_A as shown in Figure 6.1. As solar activity

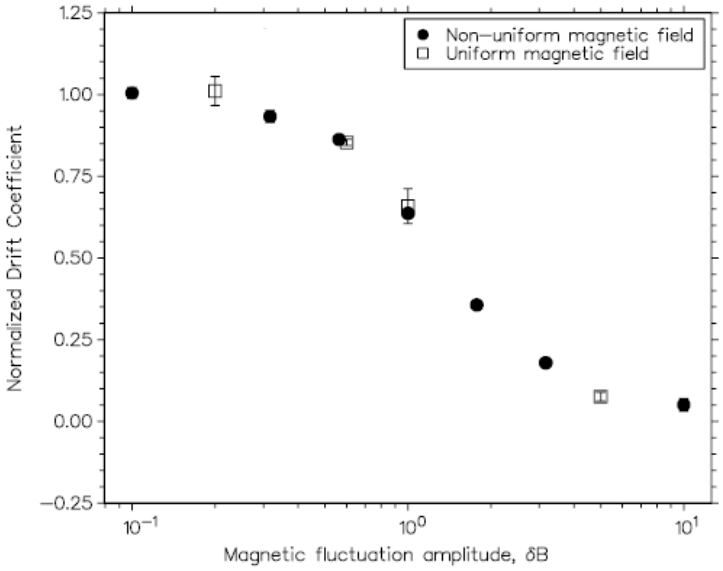

Figure 6.1: Drift coefficient K_A as a function of magnetic fluctuation amplitude δB. From *Minnie et al.* (2007).

changes over time so does δB^2. In this work, a similar dependence for the drift coefficient on solar activity, as in *Minnie et al.* (2007), is assumed but instead of δB^2 the tilt angle α is utilised to scale K_A for increasing solar activity (see *Ferreira and Potgieter*, 2004; *Ndiitwani et al.*, 2005; *Manuel et al.*, 2011a,c). This is done to compute realistic charge-sign dependent modulation over a solar cycle as shown by *Ndiitwani et al.* (2005). They showed that K_A needs to be scaled even to almost zero for extreme solar maximum periods while for solar minimum periods, $K_A \rightarrow 100\%$. This is done by constructing a simple function $f_1(t)$ which uses α as input parameter, with all α assumed to be less than 75^o. The drift coefficient, $K_A \propto f_1(t)$ and for the function $f_1(t)$, it is assumed that

$$f_1(t) = 0.013 \times \frac{(75.0^o - \alpha(t))}{\alpha_c}, \tag{6.11}$$

with $\alpha_c = 1^o$. See also *Ndiitwani et al.* (2005) and *Magidimisha* (2011). Utilising this time-dependence, the Equation 3.45 can be modified as

$$K_A = K_{A0}\frac{\beta P}{3B}\frac{\left(\frac{P}{P^*}\right)^2}{\left[\left(\frac{P}{P^*}\right)^2 + 1\right]} f_1(t), \tag{6.12}$$

where $P^* = \dfrac{1}{\sqrt{10}}$GV.

6.3 Input parameters used in the model

To calculate cosmic ray intensities, the functions $f_2(t)$ and $f_3(t)$ require B and δB^2 as input parameters which are shown in the top panel of Figure 6.2. Shown here is the OMNI magnetic field observations until 2012 (from http://cohoweb.gsfc.nasa.gov) represented

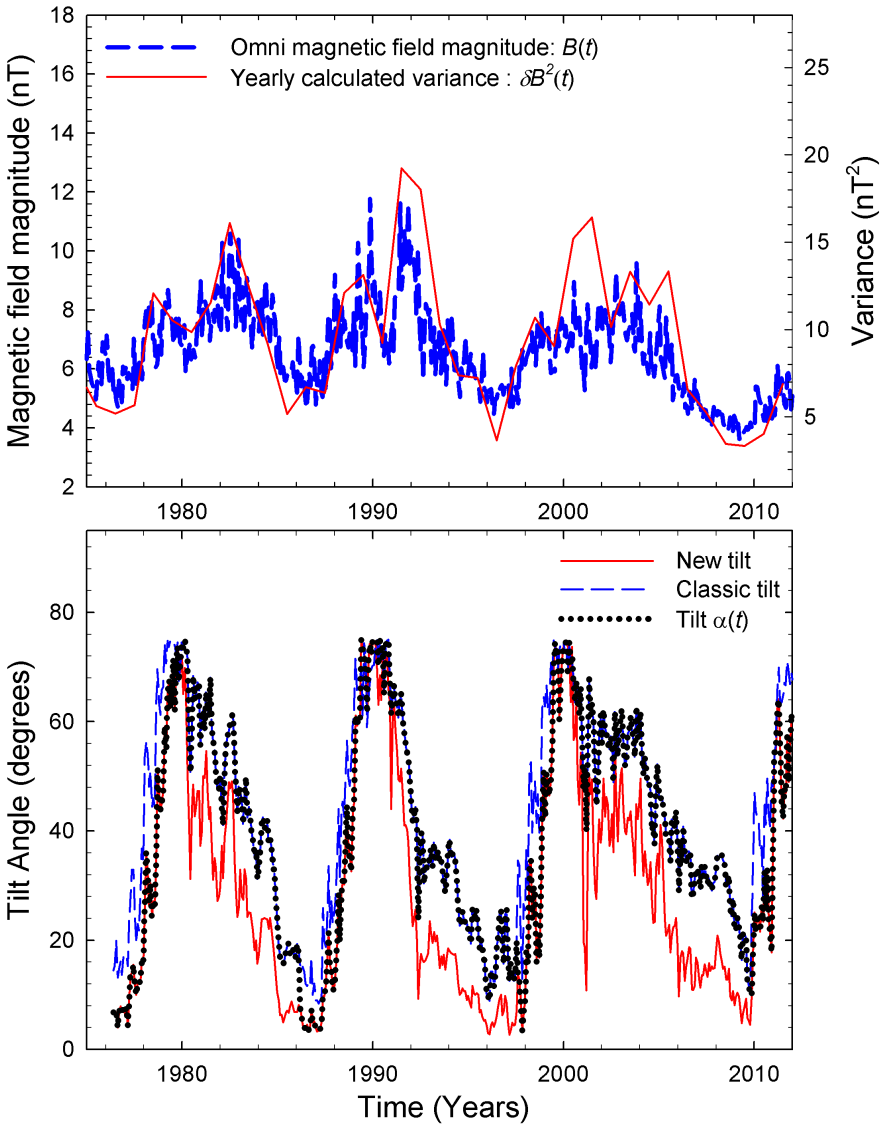

Figure 6.2: The top panel shows the observed HMF magnitude at Earth (from NSSDC COHOWeb: http://nssdc.gfc.nasa.gov/cohoweb) and the calculated yearly statistical variance. The bottom panel shows the tilt angle as a function of time (see Wilcox Solar Observatory: http://wso.stanford.edu) based on two different tilt angle models using different boundary conditions, namely the "new" (red solid line) and the "classic" (blue dashed line) model (*Hoeksema*, 1992) and the tilt angle used in the model (black dotted line).

by a blue dashed line. The total variance, δB^2, was calculated using the OMNI data. The observed hourly averages of the total field magnitude were binned in 1 year intervals, and then the statistical variance in each interval was calculated until 2012 (*Strauss*, 2010), which is shown as the red solid line in the top panel of Figure 6.2. Therefore δB^2 scales as B throughout the heliosphere. Note that these values may change over the termination shock because the magnetic field changes its character after passing through the termination shock.

Shown in the bottom panel of Figure 6.2 is the computed tilt angle (*Hoeksema*, 1992) (see Wilcox Solar Observatory: http://wso.stanford.edu) values for two different models using dif-

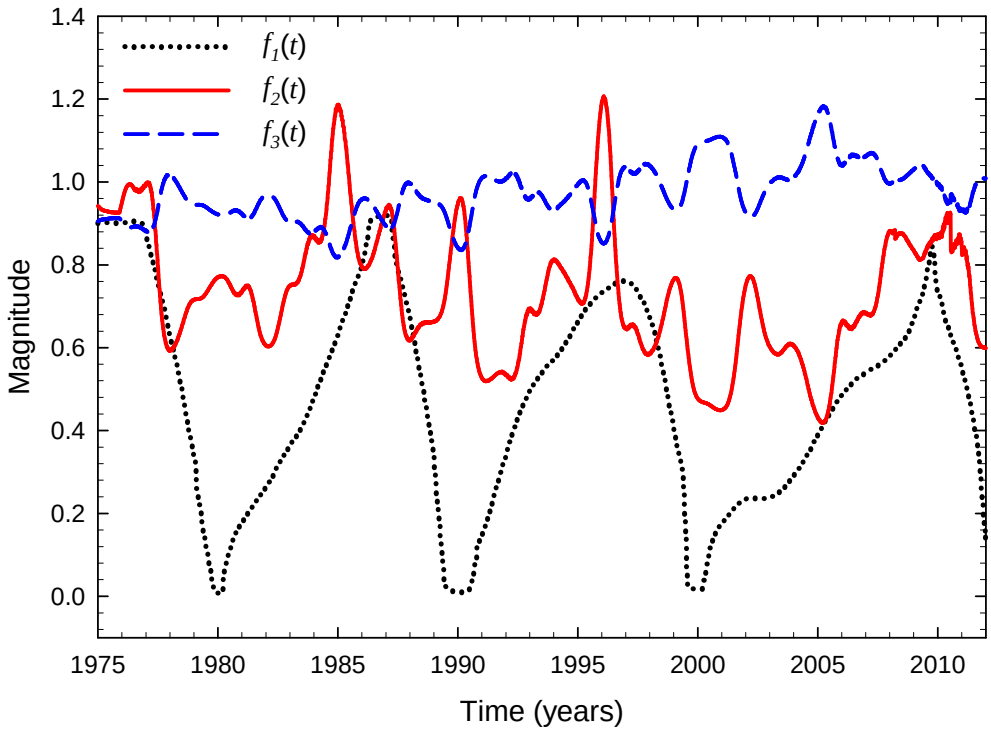

Figure 6.3: Shows the time-dependent functions $f_1(t)$ in Equation 6.11 as dotted black line, $f_2(t)$ in Equation 6.5 as solid red line and $f_3(t)$ in Equation 6.10 as dashed blue line.

ferent boundary conditions namely the "new" and the "classic" model (see Chapter 2, Section 2.8). This is shown as the solid red line and dash blue line respectively. *Ferreira and Potgieter* (2003, 2004) found that the model with the smallest rate of change in α over a period of decreasing or increasing solar activity produce optimal model results when compared to cosmic ray observations. Taking that into consideration, it is assumed for periods of increasing solar activity (1976-1980, 1986-1990, 1998-2000 and 2010-2012) the "new" tilt angle model is used, while for periods of decreasing solar activity (1980-1986, 1990-1998 and 2000-2010) the "classic" tilt angle model is used which is shown in the bottom panel of Figure 6.2 as a dotted black line.

The time-dependent function $f_1(t)$ in the drift coefficient which uses α as input parameter is shown in Figure 6.3 (dotted black line) and varies with solar activity, from $\sim$0 during solar maximum to $\sim$0.9 for solar minimum period. Also shown in Figure 6.3 is the time-dependence in the parallel and perpendicular diffusion coefficients which is produced by the functions $f_2(t)$ in Equation 6.5 (solid red line) and $f_3(t)$ in Equation 6.10 (dashed blue line) using the input parameters B and δB^2 shown in Figure 6.2. These functions vary over a solar cycle with $f_2(t)$, which determines the time-dependent changes in the parallel diffusion coefficient, resulting in an amplitude between solar minimum and solar maximum by a factor of $\sim$2 while $f_3(t)$, which is responsible for time-dependent changes in the perpendicular coefficients, only

changes by a factor of ∼1.2 between solar minimum and maximum.

Due to the particular numerical scheme used in this model, all time-dependent effects are transported radially out with the solar wind speed. For solar minimum conditions, this radial speed varies from 400 km.s^{-1} in the equatorial regions to 800 km.s^{-1} at the poles while for solar maximum conditions the speed is 400 km.s^{-1} at all latitudes (see e.g. *Ferreira and Scherer*, 2006) as discussed in Chapter 2. After the shock, the radial solar wind speed decreases according to the compression ratio of 3 (*Burlaga et al.*, 2005; *Richardson et al.*, 2008) and then decreases as $1/r^2$ further in the inner heliosheath to the heliopause (e.g. *Strauss et al.*, 2010b).

Figure 6.4 shows the solar wind profile used in the model. The top panel of the figure shows the radial profile of the solar wind speed in the heliosphere for different polar angles, while the bottom panel shows the solar wind speed at 1 AU as a function of polar angle for solar minimum and solar maximum period respectively.

Moeketsi (2004) and *Moeketsi et al.* (2005) studied the effect of different solar wind speed profiles on the distribution of 7 MeV Jovian and galactic electrons in the inner heliosphere using a 3D steady-state Jovian modulation model (*Ferreira*, 2002). These authors coupled solar wind speed to the perpendicular diffusion coefficient in the polar direction. They found that the changes in solar wind speed profile from a scenario applicable to solar minimum condition to one applicable for solar maximum condition induce changes in the spiral angle, ψ, of the HMF which lead to considerable changes in Jovian electron intensities in the inner heliosphere. Concerning the effect on galactic cosmic rays, a realistic solar wind profile was constructed by *Scherer and Ferreira* (2005a) and *Ferreira and Scherer* (2006) using a multi-fluid hydrodynamic model and it was found that the effect of large changes in the solar wind profile on the cosmic ray intensities in the inner heliosheath are negligible compared to small changes in the diffusion coefficients.

6.4 Modelling results

In this chapter the 2.5 GV results produced by the 2D time-dependent model, assuming $f_1(t)$, $f_2(t)$ and $f_3(t)$ as in Equations 6.11, 6.5 and 6.10 respectively (shown in Figure 6.3) are compared with Voyager 1, IMP 8 and Ulysses observations. Observed cosmic ray protons with kinetic energy, $E > 70$ MeV measured by Voyager 1 and IMP 8 are shown together with 2.5 GV measurements on-board the Ulysses spacecraft. As mentioned above, the aim of this chapter is not to obtain detailed fits to Voyager 1, IMP 8 and Ulysses observations, but rather to establish compatibility with these observations globally, that is to reproduce the modulation amplitude over three consecutive solar cycles at Earth and along the Voyager 1 trajectory proving whether the recent theory can reproduce to a first order long-term cosmic ray modulation.

Note that it is expected that the $E > 70$ MeV channel has a substantial contribution from anomalous cosmic ray (ACRs) protons especially in the inner heliosheath region (*Stone et al.*,

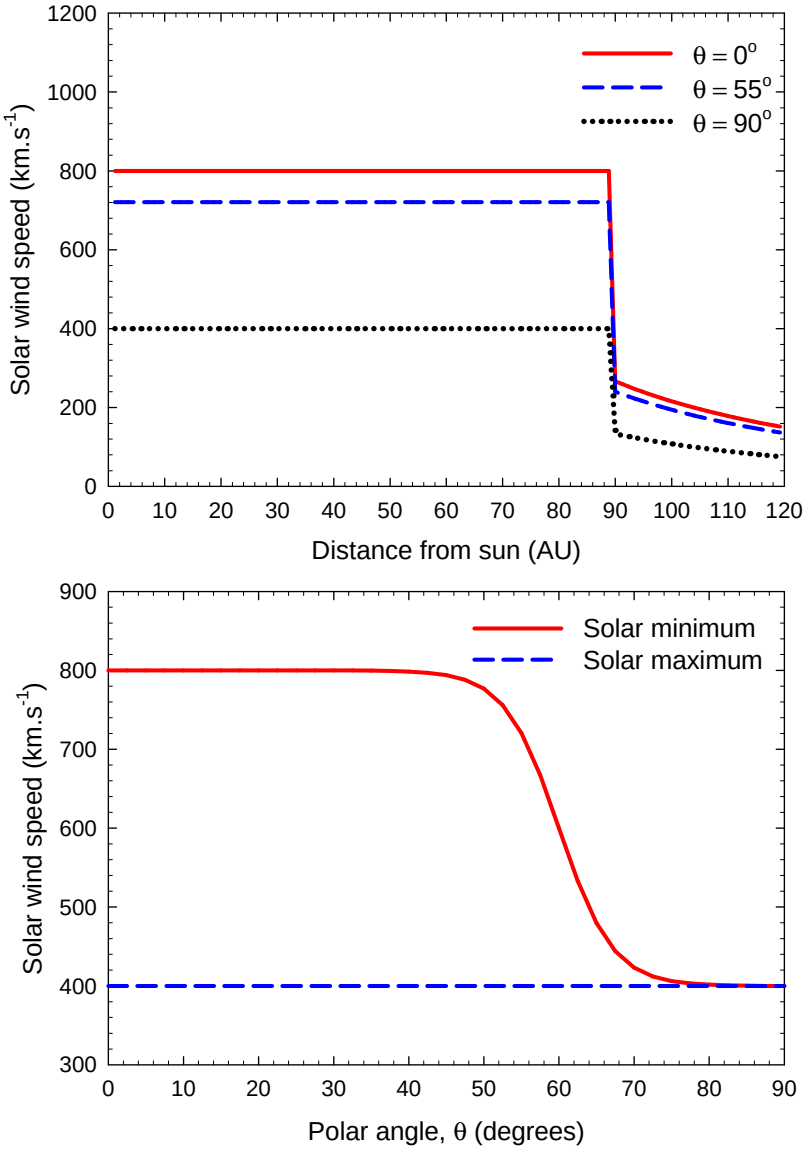

Figure 6.4: Top panel of the figure shows the radial profile of the solar wind speed for different polar angles. The bottom panel of the figure shows the solar wind speed at Earth as a function of polar angle during solar minimum and solar maximum periods. Note that this figure is only valid for a stationary interstellar medium, i.e. no relative velocity to the Sun.

2008) and therefore the observations along the Voyager 1 trajectory after 2004 should be interpreted as an upper limit when compared to galactic cosmic ray model results.

Figure 6.5 shows the $E > 70$ MeV proton observations (from http://voyager.gsfc.nasa.gov) as symbols (circles) from the Voyager 1 spacecraft as a function of time. Also shown are $E > 70$ MeV measurements at Earth from IMP 8 (from http://astro.nmsu.edu) (e.g. *Webber and Lockwood*, 1995) (triangles) and ~ 2.5 GV proton observations (squares) from Ulysses (*Heber et al.*, 2009). The Ulysses and IMP 8 observations largely agree on this global scale where they have almost the same modulation amplitude from solar minimum to solar maxi-

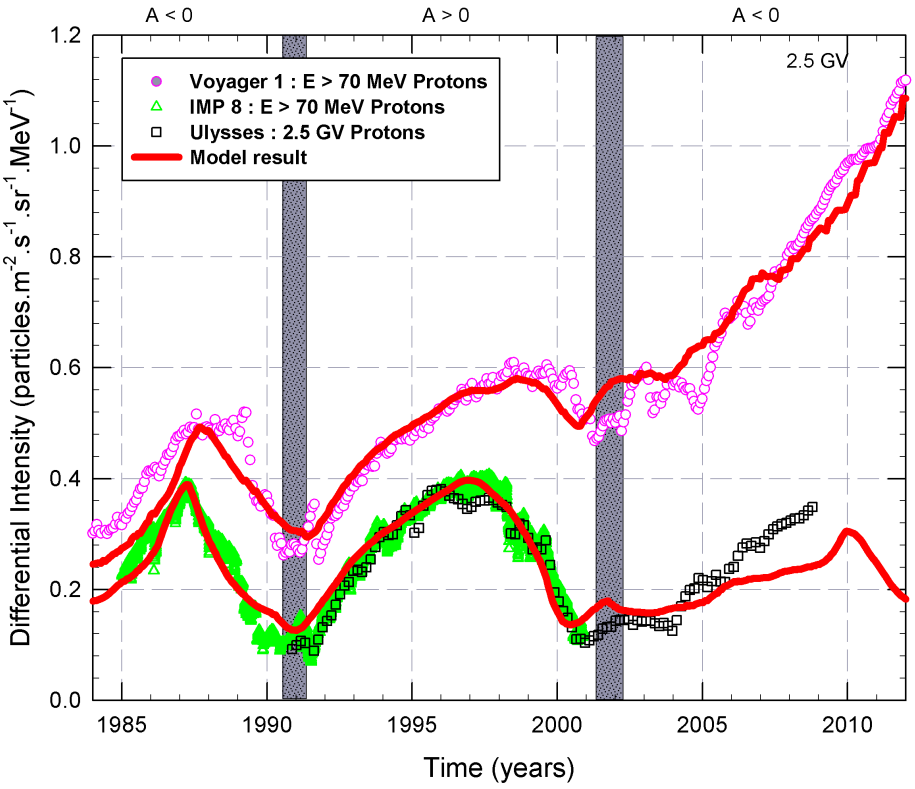

Figure 6.5: Computed 2.5 GV cosmic ray proton intensities at Earth and along the Voyager 1 trajectory since 1984 are shown as a function of time. Also shown are the proton observations from Voyager 1 $E > 70$ MeV (from http://voyager.gsfc.nasa.gov) as symbols (circles) and $E > 70$ MeV measurements at Earth from IMP 8 (from http://astro.nmsu.edu) (triangles) and $\sim$ 2.5 GV proton observations (squares) from Ulysses (*Heber et al.*, 2009). The shaded areas represent the periods where there were not a well defined HMF polarity.

mum. Note that the Ulysses spacecraft did move to higher latitudes and larger distances and therefore cannot be compared in detail with IMP 8 data without being corrected for latitudinal and radial gradients (*Heber et al.*, 2009). Since this study is mainly interested in global modulation over a solar cycle, this data-set is used only as an extension of the IMP 8 data into the recent polarity cycle to give an indication of the modulation amplitude on a global scale. For studies investigating the different latitudinal and radial gradients, and detailed comparison with Ulysses observations, see the work done by e.g. *Ferreira* (2002), *Ferreira and Potgieter* (2004) and *Ndiitwani et al.* (2005).

In Figure 6.5, computed results are shown corresponding to parameters which are optimised to fit observations in the inner and outer heliosphere. These standard parameter values are as follows: $r_{hp} = 119$ AU, $r_{ts} = 90$ AU, $a = 0.014$, $b = 0.01$, $K_{A0} = 0.8$, $C_1 = 3.0$, $C_2 = 0.8$, $k_{min} = 10^{-10}$ m^{-1} at 1 AU and the compression ratio = 3.0 (Note that some of these values are expected to change over solar cycle and these effects are fully investigated in the following chapters). The proton spectrum at 119 AU as measured by Voyager 1 is assumed at the heliopause as the HPS. Smoothed profiles of the tilt angle $\alpha(t)$, magnetic field magnitude $B(t)$ and variance

$\delta B^2(t)$ as shown in Figure 6.2 are used as input parameters.

Figure 6.5 shows that the model, assuming this standard set of parameters and time-dependence in the coefficients, as described above, produces modulation which is compatible with the observations on a global scale. This aspect was also reported by *Manuel et al.* (2011a,c). Although differences exist at certain periods (especially after ∼2004 at Earth) between the model and observations, it can be concluded that the functions $f_1(t)$, $f_2(t)$ and $f_3(t)$ and their particular dependence on δB^2, B and α result in compatible modulation over different solar and magnetic cycles and both in the inner and outer heliosphere.

However, differences between the model and observations do exist in Figure 6.5. Firstly towards solar maximum, the computed step decreases are not as pronounced as observed. This indicate that merging of diffusion barriers (*Perko and Fisk*, 1983; *Burlaga et al.*, 1993; *Le Roux and Potgieter*, 1995) should be included in the model to reproduce these periods. This is however beyond the scope of this study. Secondly, for the period ∼1984-∼1987, the model computed lower intensities than observed by Voyager 1 and for the period ∼1988-∼1990, the model is decreasing faster towards solar maximum compared to the observations. This aspect where the model over-estimates the onset of solar maximum was discussed by *Ferreira* (2002).

The most notable difference between the model and observations in Figure 6.5 are after ∼2004 at Earth. Although for this period the model results in compatible intensities along the Voyager 1 trajectory, and at Earth the computed intensities are recovering much slower towards solar minimum than observed. This aspect is now further investigated by first illustrating the effect of different parameters on the computed intensities to establish if one of these parameter could lead to improved compatibility.

6.4.1 Effect of different heliopause positions

The computed cosmic ray intensities corresponding to different heliopause radii, r_{hp}, are shown in Figure 6.6. The discussion of Figure 6.6 starts with the dashed blue line, which is considered as the optimal result compared to the observations and shown in the previous figure. For this model the modulation boundary is assumed at 119 AU which results in optimal compatibility with the observations. Note that this choice of the assumed heliopause position in the model is in general accordance to the recent Voyager 1 observations (*Krimigis et al.*, 2011) where it is predicted as 121^{-11}_{+16} AU. Also computations corresponding to a 125 AU boundary is assumed which is also within this range. This value is in accordance with the hydrodynamic simulations of the heliospheric interface done by *Scherer and Ferreira* (2005a,b). They calculated that along the trajectory of Voyager 1, the heliopause distance r_{hp} = 125 AU. They solved the well-known Euler conservation laws for a multifluid heliosphere in the meridional plane, also including the fast solar wind for solar minimum conditions (see also *Ferreira et al.*, 2007a,b). Also shown in Figure 6.6 is a theoretical case where the boundary is assumed at 115 AU to illustrate the effect of a much smaller boundary on cosmic ray modulation.

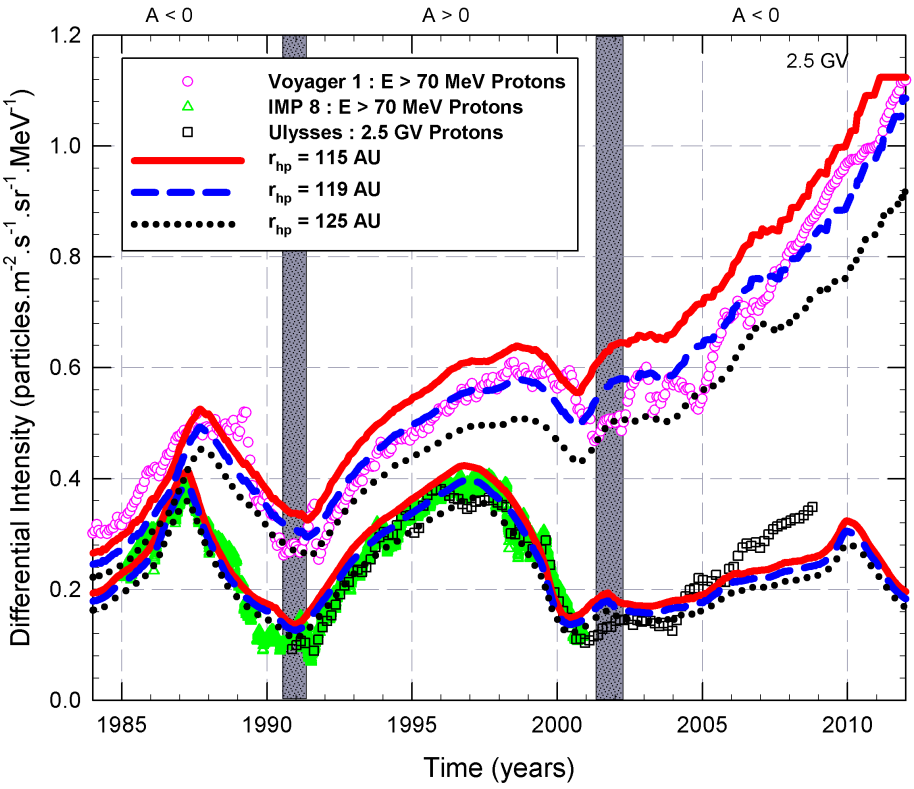

Figure 6.6: Computed 2.5 GV cosmic ray proton intensities at Earth and along the Voyager 1 trajectory since 1984 are shown for three different heliopause, r_{hp}, radii as a function of time. Also shown are the $E > 70$ MeV proton observations from Voyager 1 (from http://voyager.gsfc.nasa.gov) as symbols (circles) and $E > 70$ MeV measurements at Earth from IMP 8 (from http://astro.nmsu.edu) (triangles) and $\sim$2.5 GV proton observations (squares) from Ulysses (*Heber et al.*, 2009). The shaded areas represent the periods where there were not a well defined HMF polarity.

From the three different heliopause scenarios, it is shown that when the heliopause position is increased from 115 AU to 125 AU and keeping all other parameters in the model the same, the calculated cosmic ray intensities are decreased at Earth and along the Voyager 1 trajectory. This effect is much pronounced along the Voyager 1 trajectory especially as the spacecraft approaches the boundary. Along the Voyager 1 trajectory for the r_{hp}= 115 AU scenario the model calculated compatible results for the period $\sim$1986–1989 but afterwards the r_{hp}= 115 AU scenario is much higher than the observations. Meanwhile, the 125 AU scenario computed lower intensities than the observations, although the 125 AU scenario is compatible with results during solar maximum periods. This may indicate that from a cosmic ray perspective to compute a larger modulation amplitude, the heliopause could be situated further away from the Sun during solar maximum periods.

Comparing the different heliopause scenarios in Figure 6.6, it follows that a possible time-dep-endence in this parameter will not improve compatibility with observations at Earth after $\sim$2004. After $\sim$2004 at Earth the computed cosmic ray intensities are lower than the observations at Earth, although along the Voyager 1 trajectory the intensities are compatible. Con-

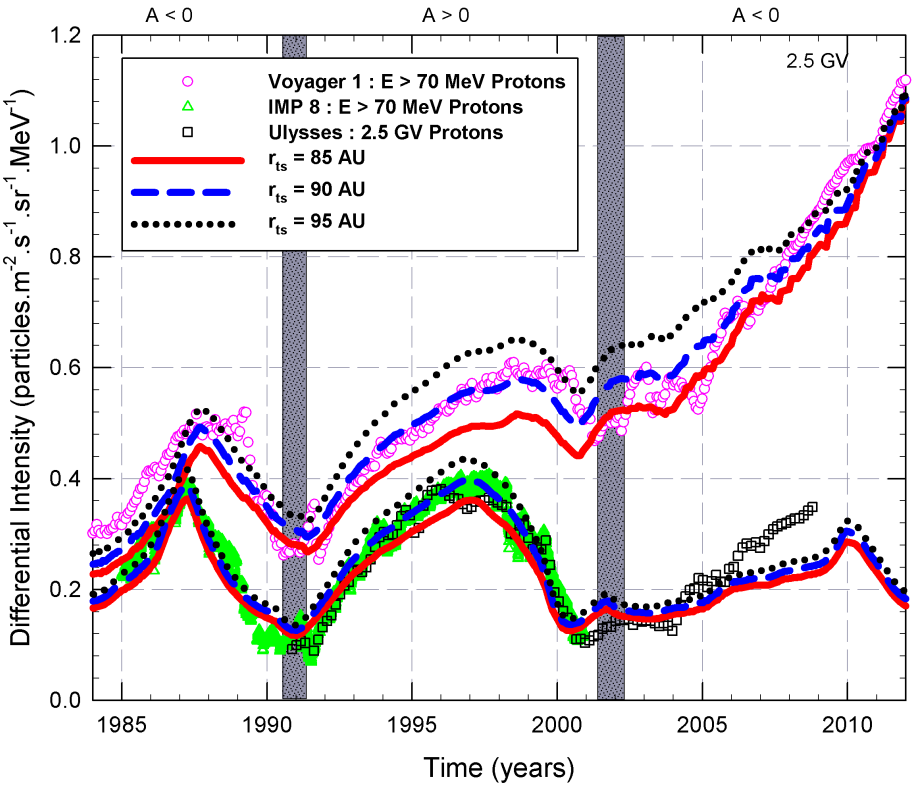

Figure 6.7: Similar to Figure 6.6 except that here model results at Earth and along the Voyager 1 trajectory are shown for different TS, r_{ts}, positions.

cluding here is that possible changes in the heliopause (boundary) position over a solar cycle may lead to improved compatibility for solar maximum periods when the model results are compared to the observations but the period from ~2004 onward is still not well fitted.

6.4.2 Effect of different termination shock positions

Figure 6.7 shows the computed results corresponding to different assumed TS positions, r_{ts}. Three different computed scenarios are shown namely $r_{ts} = 85$ AU, 90 AU and 95 AU respectively which are between what was observed by Voyager 1 and Voyager 2 (*Stone et al.*, 2005, 2008). For all three scenarios the modulation boundary r_{hp} is assumed at 119 AU. The scenario with the TS at 90 AU (dashed blue line) is assumed as the reference scenario which produces the best fit when compared to the observations. Note that the TS position is changing as a function of solar activity (*Scherer and Fahr*, 2003b; *Snyman*, 2007; *Webber and Intriligator*, 2011) and is therefore not stationary, as assumed here. The purpose of this section however is to show the sensitivity of the computed intensities on the position of the shock. In Chapter 10, a dynamic (changing over solar activity) shock position will be included in the model.

The different computed scenarios in Figure 6.7 show that a change in the r_{ts} position has a significant effect on cosmic ray intensities along the Voyager 1 trajectory when compared to

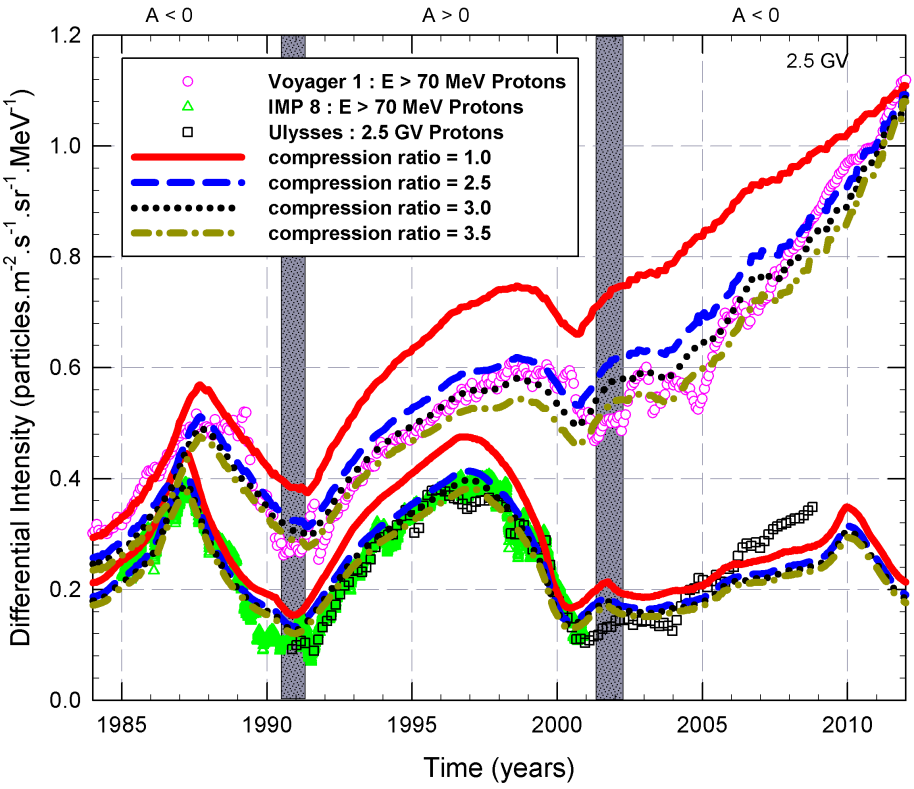

Figure 6.8: Similar to Figure 6.6 except that here model results at Earth and along the Voyager 1 trajectory are shown for different compression ratios.

the Earth. Also, it shows that at Earth during solar maximum, the different scenarios produce almost the same result. However, for solar minimum when r_{ts} is decreased, the cosmic ray intensities also decrease. This effect is much more prominent along the Voyager 1 trajectory, where it is shown that when the thickness of the inner heliosheath is decreased (e.g. increasing r_{ts} but keeping r_{hp} the same), cosmic ray intensities in the heliosphere as a whole increase. Although there is no acceleration of cosmic rays assumed in this model, the effect of the inner heliosheath is simulated by changing (decreasing) the transport parameters across the TS. This means that the inner heliosheath acts as a modulation barrier (*Potgieter and Le Roux*, 1989; *Ferreira et al.*, 2004; *Langner et al.*, 2004; *Ngobeni and Potgieter*, 2010, 2011) and increasing the thickness will result in less cosmic rays entering the heliosphere. Figure 6.7 shows that a time-dependence in the TS position is also not the answer to compute compatible results for the intensities after ∼2004, but may lead to improved compatibility at other periods.

6.4.3 Effect of different compression ratios

The compression ratio s_k is the factor by which the solar wind speed decreases across the TS. From magnetic field measurements on-board Voyager 1 spacecraft, *Burlaga et al.* (2005) reported that the value of s_k is ∼2 to ∼4 and from solar wind speed measurements on Voyager

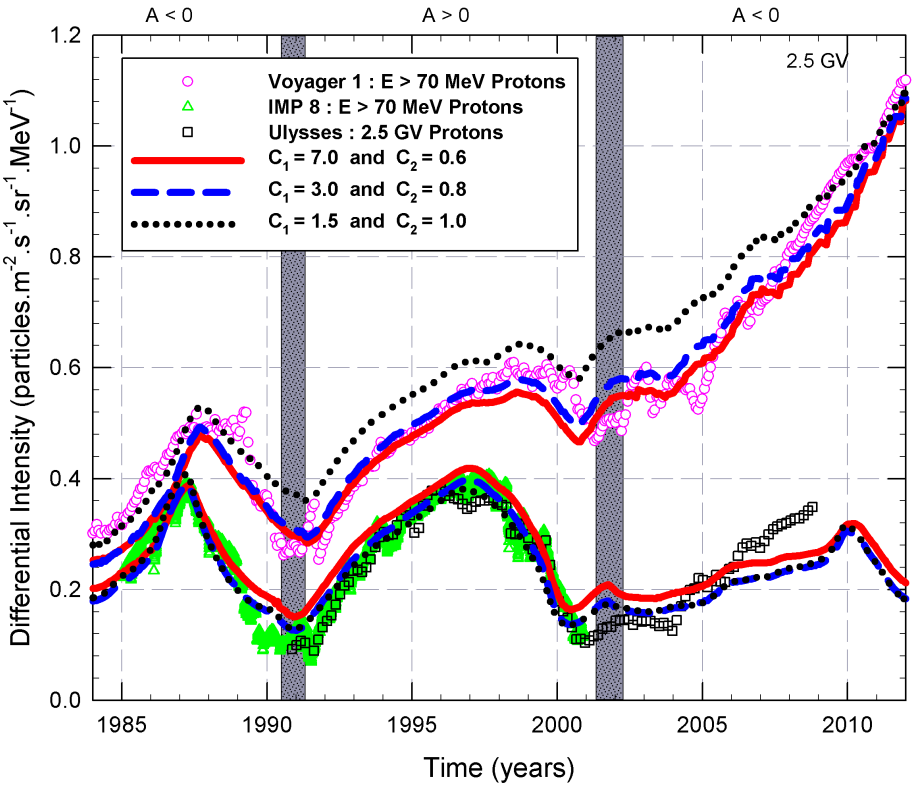

Figure 6.9: Similar to Figure 6.6 except that here model results at Earth and along the Voyager 1 trajectory are shown for different C_1 and C_2 values, as given in Equations 6.1 and 6.2.

2 spacecraft *Richardson et al.* (2008) found that s_k is ∼1.6 to ∼2.4. See also *Scherer et al.* (2006a) where it is shown how the compression ratio changes over latitude and time. In the model, the transport coefficients are decreased over the shock by this ratio. Due to measured uncertainties, the effect of different values of compression ratio is illustrated in Figure 6.8.

Figure 6.8 shows how the value of s_k effects cosmic ray modulation in the heliosphere without allowing shock acceleration. Here s_k is varied form 1.0 representing no shock scenario to 3.5. When there is no shock ($s_k = 1$), the computed cosmic ray intensity at Earth and along the Voyager 1 is higher than what is observed. From a modelling point of view, this can be corrected for by changing C_1 and C_2 in Equation 6.1 as will be shown in Figure 6.9. Shown in Figure 6.8 is that there is no real qualitative differences between the $s_k = 2.5$, $s_k = 3.0$ and $s_k = 3.5$ scenarios. The figure shows that when compression ratio is increased, the computed cosmic ray intensity at Earth and along the Voyager 1 trajectory decreases. Again, after ∼2004 a change in compression ratio still could not reproduce cosmic ray intensities measured at Earth.

6.4.4 Effect of different C_1 and C_2 values

The effect of different C_1 and C_2 values, as given in Equations 6.1 and 6.2, on computed intensities is shown in Figure 6.9. The C_1 value determines the magnitude of the transport coefficients

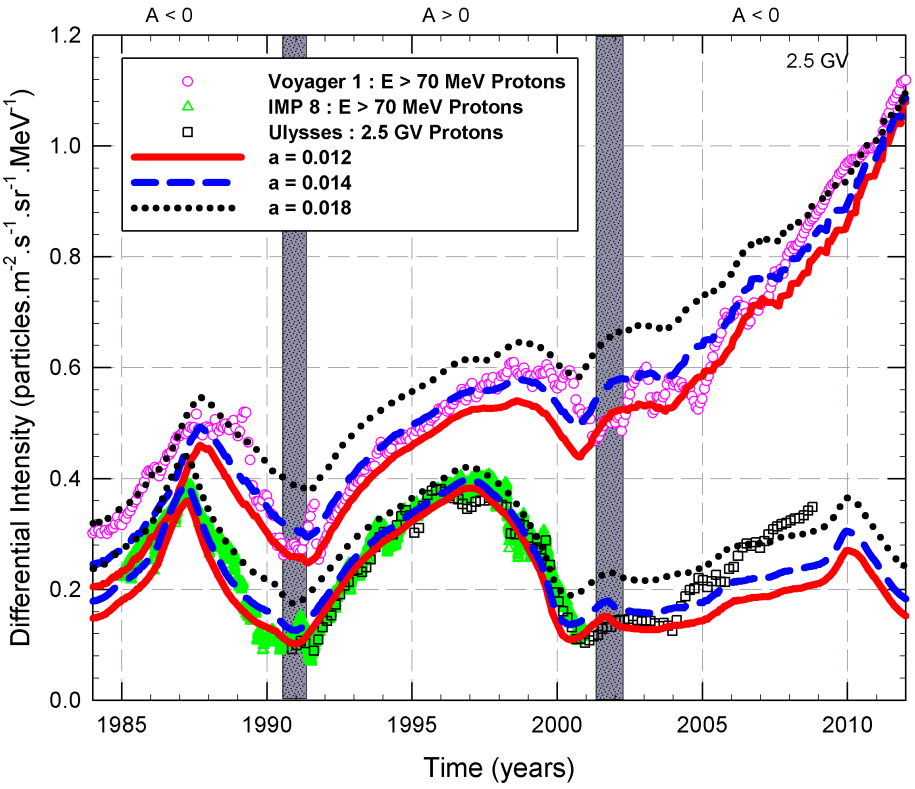

Figure 6.10: Similar to Figure 6.6 except that here computed results at Earth and along the Voyager 1 trajectory are shown for different a values, where a is the ratio of perpendicular diffusion coefficient in radial direction to the parallel diffusion coefficient as given by Equation 6.6.

at Earth and C_2 the radial dependence where $K_{||} \propto C_1 r^{C_2}$. From the figure it follows that when the radial dependence is increased from C_2 =0.6 to 1.0, the C_1 value has to be decreased from 7.0 to 1.5 to decrease the computed intensities at Earth to be compatible to the observations. This however increases the intensity along the Voyager 1 trajectory. Also, we can see that the different coefficient scenarios fit the observations better for different solar cycles, e.g. during 1985–1990 A<0 cycle, C_1 =1.5 and C_2 =1.0 result in a better fit compared to the observations than the other two scenarios, but during 1991–2001 A>0 cycle, C_1 =3.0 and C_2 =0.8 result in a better fit to the observations. This suggests that different diffusion coefficients can be assumed for different polarity cycles (e.g. *Reinecke et al.*, 1996; *Burger et al.*, 2000; *Potgieter*, 2000; *Ferreira*, 2002) to result in an improved compatibility when compared to the observations. However, C_1 =3.0 and C_2 =0.8 are considered as an overall best fit scenario. Again after ~2004, all the different scenarios fail to reproduce the cosmic ray observations at Earth.

6.4.5 Effect of different a values

The effects on computed intensities of the ratio of perpendicular diffusion coefficient in the radial direction to the parallel diffusion coefficient, a, as given in Equation 6.6, is shown in

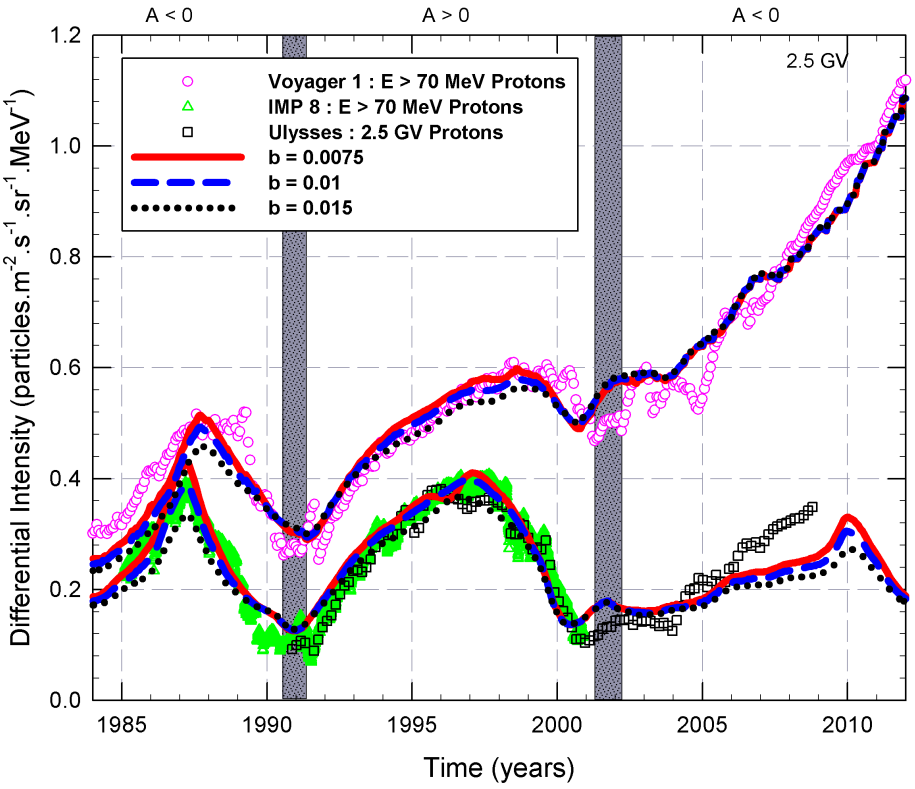

Figure 6.11: Similar to Figure 6.6 except that here computed results at Earth and along the Voyager 1 trajectory are shown for different b values, where b is the ratio of the perpendicular diffusion coefficient in the polar direction to parallel diffusion coefficient in the equatorial plane as described by Equation 6.7.

Figure 6.10. Three different scenarios corresponding to $a = 0.012$, 0.014 and 0.018 in the model are shown with the value 0.014 considered as the optimal value when compared to observations. When the a value is increased, the cosmic ray intensities inside the heliosphere increase because of the larger perpendicular diffusion coefficient. This is evident at Earth and along the Voyager 1 trajectory. When compared to the observations, for the period 1985–1989 during an A<0 polarity cycle, the $a = 0.018$ scenario produces an optimal result when compared to the observations. However, when compared to observations during solar maximum periods, a smaller a value (0.012) produces a more compatible result. For the reference scenario (a =0.014), the model produces a global fit at Earth until ∼2004 as already mentioned but not thereafter. By increasing the a value to 0.018, the intensities tend to increase to observed solar minimum values at Earth but may still be too high along the Voyager 1. Figure 6.10 however suggests that a time-dependent a value may produce a better fit after ∼2004 at Earth. This suggests a different time-dependence rather than what is assumed in this work so far.

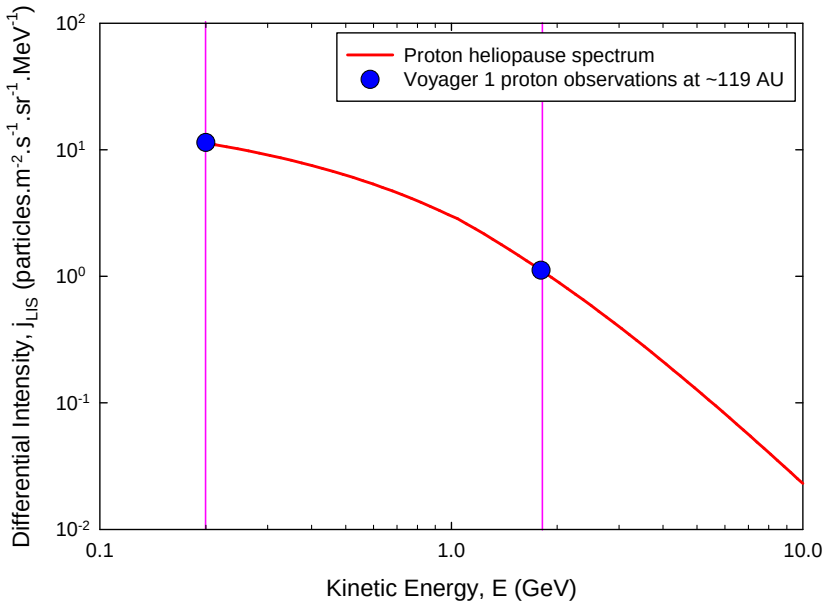

Figure 6.12: The proton HPS assumed in this study from the Voyager 1 measurements of 133-242 MeV and the integral channel >70 MeV (mean rigidity of ∼2.5 GV) protons at ∼119 AU. The vertical lines denote 200 MeV and 1.8 GeV (∼2.5 GV).

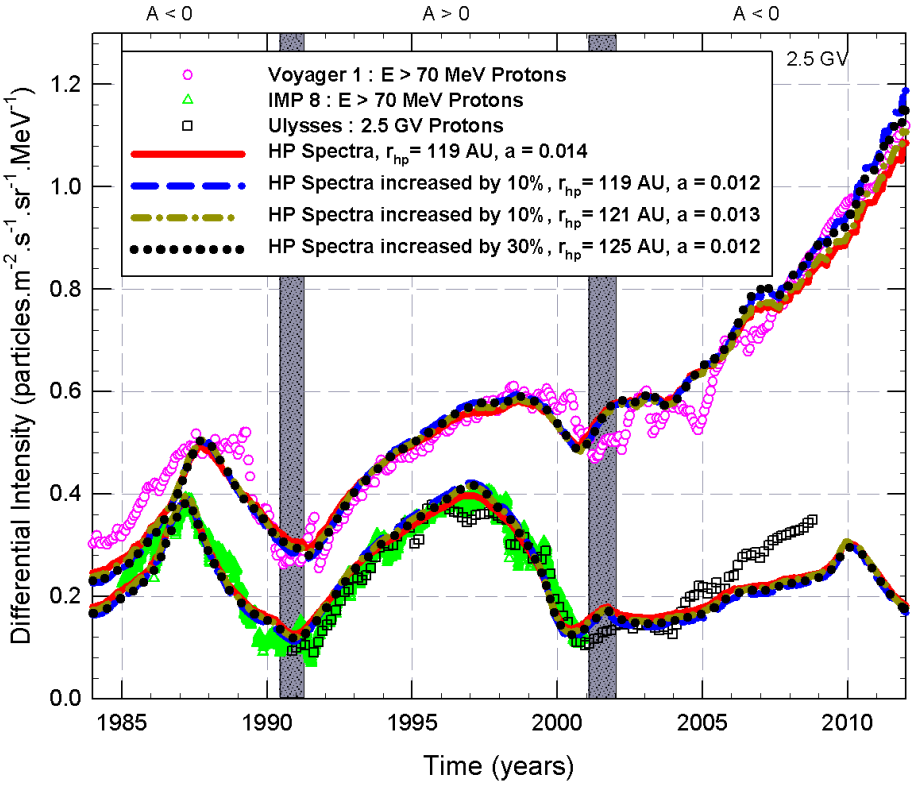

Figure 6.13: Similar to Figure 6.6 except that here model results at Earth and along the Voyager 1 trajectory are shown for the assumed HPS and for a 10 % and 30 % increase in the HPS for different a values.

6.4.6 Effect of different b values

Figure 6.11 shows computed results corresponding to different b values, which is the ratio of the perpendicular diffusion coefficient in the polar direction to parallel diffusion coefficient in the equatorial plane as given in Equation 6.7. Different scenarios corresponding to b = 0.0075, 0.010 and 0.015 are shown. As it is shown, an increase in b decreases the cosmic ray intensities slightly at Earth and along the Voyager 1 trajectory during solar minimum periods but the intensity remains almost the same during solar maximum periods. Although there is not much difference between the different solutions, the $b = 0.01$ scenario largely follows the observations and is considered as an optimal result when compared to the observations. Again, after ∼2004, the model fails to reproduce the observations at Earth for all b values considered here.

6.4.7 Effect of different heliopause spectra

For this study a HPS of protons is assumed from the 133-242 MeV and >70 MeV (∼2.5 GV) proton measurements by Voyager 1 at ∼119 AU. The intensity values of these are specified at the heliospheric modulation boundary (heliopause) as a HPS. The assumed proton HPS is shown in Figure 6.12 with the two energy and intensity values indicated. Note that modulation beyond the heliopause may occur (as mentioned in Chapter 2 and reported on by *Scherer et al.* (2011)) but this effect is not included in the model. In order to illustrate the effects of a possible higher HPS the assumed HPS (as in all previous figures) was increased by 10% and then by 30% respectively.

Figure 6.13 shows four computed cosmic ray intensity scenarios. The solid red line represents the reference scenario with the assumed HPS at 119 AU and an $a = 0.014$. The dashed blue line represents the scenario where the assumed HPS is increased by 10%, and the heliopause assumed at 119 AU and a decreased $a = 0.012$ to compute compatibility. The computed scenario in this case follows the reference scenario until ∼2010. After ∼2010, this scenario computed higher intensities along the Voyager 1 trajectory. The third scenario is represented by dash-dotted yellow line, where the assumed HPS is increased by 10% but with an increased heliopause position i.e. 121 AU and $a = 0.013$ assumed in the model. The computed result for this scenario also follows the reference scenario. Also a fourth scenario represented by a dotted black line shows a 30% increased HPS assumed at 125 AU and $a = 0.012$, which again follows the reference scenario. From this it follows that an increase in the HPS compared to the reference scenario could also result in realistic cosmic ray modulation if the heliopause position is increased accordingly and/or by changing the diffusion coefficients. Therefore possible differences from what is assumed in this work as a HPS and the true HPS will not lead to different conclusion.

6.5 Summary and conclusions

A well established time-dependent cosmic ray modulation model was utilised to compute long-term cosmic ray modulation over multiple consecutive solar and magnetic cycles. Results were compared to Voyager 1, Ulysses and IMP 8 proton observations to establish whether the parameters assumed in this work result in realistic computed intensities. The current sheet tilt angle values and magnetic field magnitude measurements at Earth were used as input for the model. Also a statistical variance in the magnetic field were calculated and with the measured magnetic field used to construct a time-dependence in the transport parameters as given in recent theoretical studies by *Teufel and Schlickeiser* (2002, 2003), *Shalchi et al.* (2004) and *Minnie et al.* (2007). This time-dependence is then transported out into the simulated heliosphere resulting in model calculations compatible to observed cosmic ray intensities on a global scale. This approach also compares well to the previous compound approach of *Ferreira* (2002) and *Ferreira and Potgieter* (2004) until ∼2004 at Earth.

This new approach successfully computed cosmic ray intensities along the Voyager 1 trajectory which are compatible to Voyager 1 observations until 2012 and also computed intensities at Earth which are compatible to the IMP 8 and Ulysses observations until ∼2004. However, after ∼2004 at Earth the model results failed to reproduce the observations and computed lower intensities than observed. A thorough parameter study was conducted by testing the effects of different parameters like the heliopause position, TS position, compression ratio, different diffusion coefficients etc., on the computed cosmic ray intensities. It was shown that expected solar-cycle related changes in these parameters do not lead to improved compatibility with the data for the period after ∼2004 at Earth. Indeed these calculations suggested a need to modify the assumed time-dependence in diffusion coefficients, which is the topic of the next chapter. Lastly, it was found that variations in the HPS compared to what is assumed in this work can always be compensated for by an increased heliopause position and/or by changing the diffusion coefficients.